PCCP

PAPER

View Article Online
View Journal | View Issue



Cite this: *Phys. Chem. Chem. Phys.*, 2025, **27**, 11898

# Influence of imide side-chain functionality in the doping characteristics of naphthalenediimide derivatives as electron transport materials†

Wai Kin Yiu, Lewis Mackenzie, Dylan Wilkinson, Marcin Giza, Benjamin Vella, Michele Cariello, Stephen Sproules, Graeme Cooke * and Pablo Docampo *

Achieving effective doping in n-type organic molecular charge transport materials is critical for the development of high-performance optoelectronic devices. However, the role of side-chains in doping reactions remains incompletely understood in some systems. This study focuses on naphthalenediimide (**NDI**) derivatives, which offer simple synthetic protocols and potentially lower costs compared to traditional fullerene-derived materials. In particular, we explore two functionalised **NDI** derivatives, comparing one with polar ethylene glycol side-chains (**NDI-G**) to a non-polar variant with branched alkyl side-chains (**NDI-EtHx**). Our results show that the effectiveness and speed of the doping reaction with (4-(1,3-dimethyl-2,3-dihydro-1*H*-benzoimidazol-2-yl)phenyl)dimethylamine (**N-DMBI**) is much higher with the more polar **NDI-G** derivative. We postulate that this arises partly from the closer interactions between the dopant and the **NDI** molecule, facilitated by the polar glycol side-chains. As a result, thin films reach conductivities exceeding $10^{-2}$ S cm$^{-1}$. We additionally demonstrate their incorporation into efficient perovskite solar cells, demonstrating the effectiveness of the doping process. We investigate this process with a combination of spectroscopy and density functional theory (DFT) modelling, showing that a complex is likely formed between the resulting **N-DMBI** cation and the **NDI** radical anion which then promotes electron transfer to a neutral **NDI** molecule, thereby generating free charge in the film. These findings underscore the importance of synthetic design on the doping behaviour, with the incorporation of ethylene glycol side-chains emerging as an effective strategy to achieve better electrical conductivity for NDI based systems.

Received 3rd March 2025,
Accepted 12th May 2025

DOI: 10.1039/d5cp00828j

rsc.li/pccp



## Introduction

Doping is an effective approach to enhance the conductivity of organic semiconductors by generating free charges through interactions between dopant species and the host organic semiconductor.[1] This method has been particularly effective in fullerene-based electron transport materials (ETMs) such as $C_{60}$ and phenyl-$C_{61}$-butyric acid methyl ester (**PCBM**), enabling conductivities exceeding 10 S cm$^{-1}$.[2] However, achieving optimal doping is essential to meet the requirements of specific device applications. For instance, excessively high conductivity in transistors can lead to current leakage and reduced low on/off ratios,[3] which explains why doped fullerene ETMs in perovskite solar cells typically exhibit conductivity within the range of $10^{-3}$–$10^{-4}$ S cm$^{-1}$.[4,5] Recently, there has been increasing interest in non-fullerene alternatives such as naphthalenediimide (**NDI**) derivatives due to their simpler synthesis and tuneable energy levels.[6–8] These characteristics contribute to reduced chemical usage, lower energy consumption, and decreased production costs. While n-type doping has improved **NDI** conductivity up to $10^{-1}$ S cm$^{-1}$,[9] the doping mechanism in these systems is not yet fully understood.[1]

**NDI**-based materials face challenges with poor solubility in organic solvents, resulting in poor film morphology and an increased density of defects.[10,11] These defects can act as trapping sites for charge carriers, hindering efficient charge transport.[12,13] The solubility issue of **NDI**-based molecules can be addressed by synthetically modifying the imide or naphthalene unit side-chains, which do not require complicated synthesis procedures.[14,15] These simple modifications, however, can also impact the material's optoelectronic properties.[16,17] For instance, Liu *et al.* demonstrated that the polarity and the length of glycol side-chain in fullerene derivatives influence

*School of Chemistry, University of Glasgow, Glasgow, G12 8QQ, UK.*
*E-mail: Graeme.Cooke@glasgow.ac.uk, Pablo.Docampo@glasgow.ac.uk*

† Electronic supplementary information (ESI) available. See DOI: https://doi.org/10.1039/d5cp00828j

performance in n-type organic thermoelectric materials,[16] and Vijayakumar *et al.* investigated how the length of alkyl side-chain affects doping kinetics and charge transport properties in poly(2,5-bis(3-alkylthiophen-2-yl)thieno[3,2-*b*]thiophene) (**PBTTT**) films.[18] A systematic investigation of how different side-chains affect the reactivity between host molecules and molecular dopants is generally lacking. Further research is needed to understand how specific synthetic modifications, particularly the choice of side-chains, not only enhance solubility in solvent, but also influence the local doping environment and control the doping behaviour.

In this study, we have developed two **NDI**-based molecules featuring ethylene glycol (**NDI-G**) and ethylhexyl (**NDI-EtHx**) side-chains. Both moieties enhance the solubility in organic solvents but exhibit different reaction kinetics upon addition of (4-(1,3-dimethyl-2,3-dihydro-1*H*-benzoimidazol-2-yl)phenyl)-dimethylamine (**N-DMBI**) as the n-type dopant. We investigate the origin of the conductivity differences of doped and undoped species as well as the optical and redox properties of these systems. We use UV-vis spectroscopy and cyclic voltammetry (CV), together with density functional theory (DFT) modelling to probe the doping process of NDI derivatives with **N-DMBI**. Utilising UV-vis and conductivity measurements, we have shown that **NDI-G** exhibited a more effective doping reaction with **N-DMBI**, resulting in shorter doping times and superior conductivity. Lastly, we have fabricated perovskite solar cells using **NDI-G** and **NDI-EtHx** as ETLs and report that the choice of side-chain critically impacts device performance.

## Results and discussion

In this work, we focus on the impact of the side-chain environment around **NDI** derivatives has on the doping efficiency with **N-DMBI**. We postulate that manipulating the polarity of side-chains attached to the molecules will allow the control of the effectiveness and rate of the doping reaction. Here, we have attached an ethylene glycol side-chain to create a more polar environment in the **NDI-G** derivative, while an ethylhexyl side-chain was incorporated in **NDI-EtHx** to create a less polar one.

The full synthesis of **NDI-G** and **NDI-EtHx** is reported in the ESI† and chemical structures of **NDI-G**, **NDI-EtHx**, and **N-DMBI** are shown in Fig. 1a. The solution optical properties of **NDI-G** and **NDI-EtHx** were evaluated using UV-vis spectroscopy to characterise the effect of the side-chain functionalisation has on the light absorption properties. Our results show similar spectra for both molecules with no significant influence of side-chains, see Fig. 1b, indicating that this type of functionalization does not significantly influence the electronic properties of their 'as-synthesised' form.

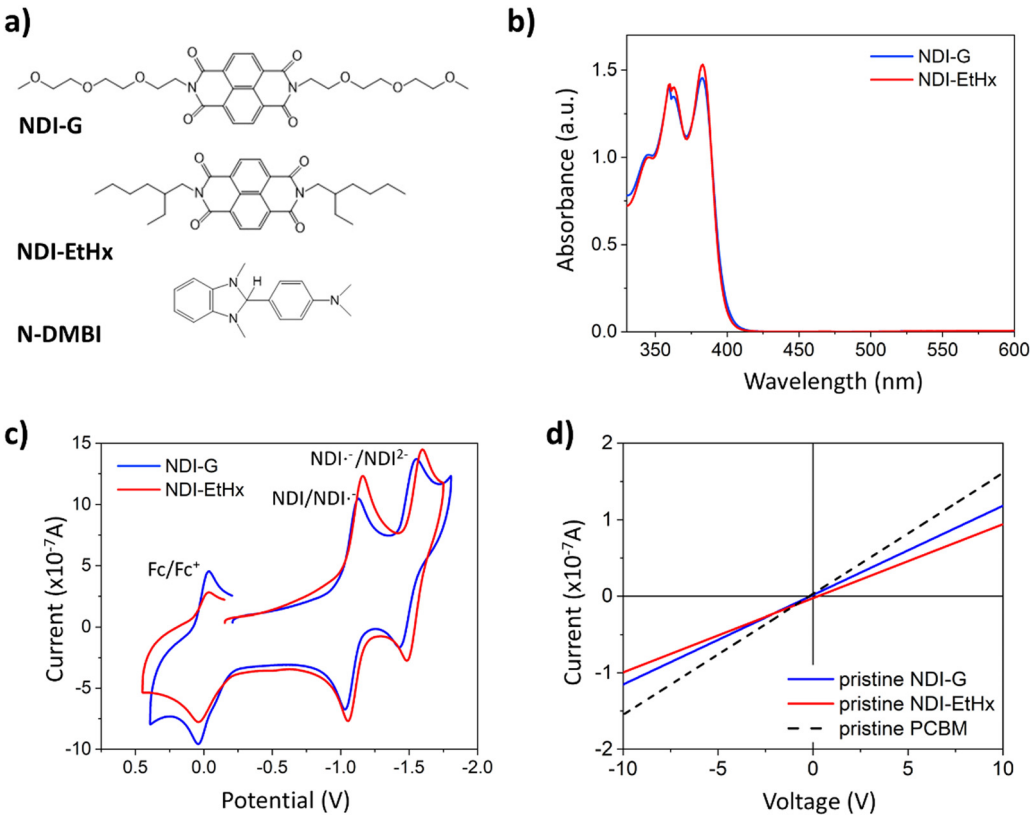


Fig. 1 (a) Structures of **NDI-G**, **NDI-EtHx** and **N-DMBI**; (b) solution UV-vis absorption spectra of pristine **NDI-G** and **NDI-EtHx** in chlorobenzene, $1 \times 10^{-5}$ M; (c) cyclic voltammetry measurements of **NDI-G** and **NDI-EtHx** with ferrocene as reference ($1 \times 10^{-4}$ M in $CH_2Cl_2$; scan rate 0.1 mV $s^{-1}$); and (d) conductivity measurements of pristine **NDI-G**, **NDI-EtHx** and **PCBM** self-doped in air.

CV was used to determine the solution redox properties of **NDI-G** and **NDI-EtHx** (Fig. 1c), as well as the dopant, **N-DMBI** (Fig. S6, ESI†). Both **NDI** derivatives exhibited two pseudoreversible reduction waves by comparing with ferrocene as internal reference. The redox waves correspond to two one-electron reductions forming radical anion and dianion states, respectively. The estimated electron affinities (EAs) of **NDI-G** and **NDI-EtHx** are −3.67 eV and −3.70 eV, respectively, which are shallower than **PCBM** (−3.92 eV).[19]

DFT calculations were performed on an analogue of **NDI-G** and **NDI-EtHx**, in which the side chain groups were truncated to methyl units (**methyl-NDI**) to simplify the systems, facilitate convergence of the geometry optimisations, and focus on the interaction between the dopants and the core **NDI** moiety. This adjustment is based on the minimal effect that side-chains generally have on the electronic properties of the NDI core.[20] The gas phase highest occupied molecular orbital (HOMO) and lowest unoccupied molecular orbital (LUMO) levels of **methyl-NDI** were calculated to be −7.22 eV and −3.56 eV, respectively. In combination with the CV results, this indicates that **NDIs** have similar energy levels to fullerenes derivatives, and hence that **NDI-G** and **NDI-EtHx** have the potential to serve in a similar range of optoelectronic device applications from the point of view of energetic alignment. Conductivity was extracted from the resistance values of standard current–voltage curve employing pristine **NDI** derivatives on patterned-ITO substrates with an inter-digitated contact configuration. **NDI** derivatives exhibit lower conductivity ($\sim \times 10^{-7}$ S cm$^{-1}$) compared to **PCBM** ($1.57 \times 10^{-6}$ S cm$^{-1}$), as shown in Fig. 1d.

To enhance the conductivity of the **NDI** derivatives, **N-DMBI** has been employed as an n-type dopant. **N-DMBI** has well-documented effectiveness in catalysing the reduction of organic compounds[21] and is able to facilitate hydrogen and/or electron transfer reactions by forming radicals.[22,23] The HOMO of **N-DMBI** is −4.67 eV, which is deeper than the LUMO of **PCBM**, **NDI-G** and **NDI-EtHx**. As a result, direct electron transfer between **N-DMBI** and **NDI** derivatives is not possible due to energy level misalignment. Furthermore, C–H bond dissociation at room temperature is energetically unfavourable due to its high enthalpy change. Hence, photo[24] or thermal activation[24,25] is required for effective doping.

To confirm the **NDI** radical anion formation in the doping process, electron spin resonance (ESR) and UV-vis absorption measurements were recorded upon addition of 10 mol% and 30 mol% **N-DMBI** to **NDI-G** and **NDI-EtHx**, respectively. Upon addition of **N-DMBI**, ESR shows a strong paramagnetic signal with a g value of 2.004 and hyperfine features were observed for **NDI-EtHx**. These features were less distinct in the **NDI-G** moiety, possibly due to its larger molecular structure, which slows molecular tumbling and obscures the hyperfine details. The ESR signal further confirms the formation of an **NDI** radical anion, while there is no appreciable radical signal obtained in the pristine **NDI-G** and **NDI-EtHx** samples, as shown in Fig. 2a and b. Experimental solid-state UV-vis absorption spectra for the pristine and **N-DMBI** doped **NDI** derivatives are shown in Fig. 2c. Interestingly, the derivatives display different absorption features upon doping (*ca.* 450 nm *versus* 475 nm), suggesting that either different reduced species are being formed or that the local environment provided by the differing side-chains shifts the absorption for the **NDI** radical anion.[26,27]

Generally, the doping process in molecular electron transporters is described as a two-step process: (i) ionisation of the dopant by transferring a charge to the semi-conducting host material to form the complex and (ii) dissociation of the complex generating free charge carriers by transferring the electron to a neutral nearby host.[28] However, step (ii) is not at all obvious in an organic semiconductor due to the strong Coulombic binding energy between host material and additive.[28] Here, unlike n-dopants that undergo direct dopant to acceptor electron transfer, **N-DMBI** doping operates by a more complicated process that may be specific to the acceptor used and the conditions employed. Therefore, a single mechanism will probably not be able to account for all **N-DMBI**/acceptor combinations.[29]

The initial step for **N-DMBI** doping reactions will likely result from C–H bond cleavage and the general consensus appears to be that initial hydride [H$^-$] transfer rather than other mechanisms such as hydrogen radical [H$^\bullet$] transfer to the acceptor plays the most significant role for most **N-DMBI**/acceptor combinations.[30,31] However, the initial step is not straightforward as other studies have indicated that electron transfer may occur prior to C–H bond homolysis for powerful electron acceptors that have poor affinity for hydride or

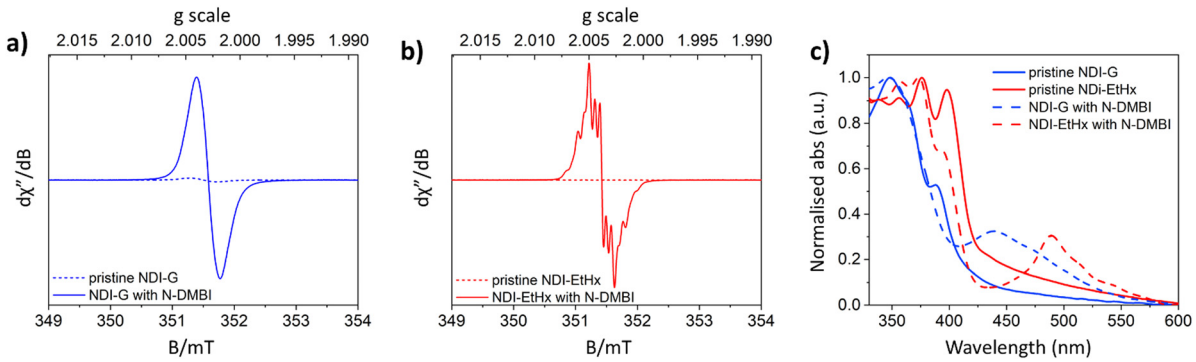


Fig. 2 X-band EPR spectrum of pristine and after addition of **N-DMBI** for (a) **NDI-G** ($3.57 \times 10^{-2}$ M) and (b) **NDI-EtHx** ($4.08 \times 10^{-2}$ M) recorded in chlorobenzene; (c) UV-vis absorption spectra of pristine and after addition of **N-DMBI** for both **NDI** derivatives ($1 \times 10^{-5}$ M).

 

hydrogen transfer.[32,33] Furthermore, when **NDI** is used as an acceptor, previous studies have shown that **N-DMBI** gives rise to very sluggish hydride transfer and that the hydrogen transfer may not be energetically favourable.[30,34,35] Nevertheless, regardless of which species is initially formed, it is clear from ESR that the radical anion states of **NDI-EtHx** and **NDI-G** are formed upon doping with **N-DMBI**. Presumably this occurs by subsequent reactions of the **NDI** hydrides (**NDI-H**$^-$) (or other species) formed initially.

DFT modelling was also used to investigate the interactions of the **N-DMBI** cation and **methyl-NDI** radical anion that likely result from the doping reaction. The electrostatic potential (ESPs) and spin density maps of the complex indicated that the negative charge is localized on more electronegative oxygen and nitrogen atoms of the **NDI** units (Fig. S7a, ESI†), and the unpaired electron is highly delocalized on the **NDI** unit (Fig. S7b, ESI†). The calculated binding energies of **[methyl-NDI**$^-$**/N-DMBI**$^+$**]**$^\bullet$ and π–π dimer of **methyl-NDI** are 56.3 kcal mol$^{-1}$ (2.44 eV) and 0.4 kcal mol$^{-1}$ (0.02 eV), respectively, showing a stronger binding force of the complex than most organic materials (typically 0.5 eV).[36] The **[methyl-NDI**$^-$**/N-DMBI**$^+$**]**$^\bullet$ is stable and the high coulombic binding energy suggests it is unlikely to dissociate into free charge carriers. We have also modelled **[NDI-G**$^-$**/N-DMBI**$^+$**]**$^\bullet$ and **[NDI-EtHx**$^-$**/N-DMBI**$^+$**]**$^\bullet$ to reveal whether the gas phase calculations can reveal any information regarding the role the side-chain moieties play in the complexation process (Fig. S8, ESI†). The calculated binding energies were slightly lower than that observed for **[methyl-NDI**$^-$**/N-DMBI**$^+$**]**$^\bullet$ (**[NDI-G**$^-$**/N-DMBI**$^+$**]**$^\bullet$ = 38.52 kcal mol$^{-1}$ (1.67 eV) and **[NDI-EtHx**$^-$**/N-DMBI**$^+$**]**$^\bullet$ = 42.57 kcal mol$^{-1}$ (1.85 eV)).

The computed energy levels of **[methyl-NDI**$^-$**/N-DMBI**$^+$**]**$^\bullet$, **[NDI-G**$^-$**/N-DMBI**$^+$**]**$^\bullet$ and **[NDI-EtHx**$^-$**/N-DMBI**$^+$**]**$^\bullet$ were compared. In all cases the calculated LUMO level of the neutral **NDI** derivative is deeper than the singly occupied molecular orbital (SOMO) of its complex with **N-DMBI**, indicating a potential for electron transfer from complex to neutral **NDI** unit, as shown in Fig. 3 and Fig. S8 (ESI†). Furthermore, the SOMO/LUMO gaps for **[NDI-G**$^-$**/N-DMBI**$^+$**]**$^\bullet$ (0.4 eV) and **[NDI-EtHx**$^-$**/N-DMBI**$^+$**]**$^\bullet$ (0.4 eV) and their respective neutral **NDI** species were slightly smaller than that obtained for **[methyl-NDI**$^-$**/N-DMBI**$^+$**]**$^\bullet$ (0.9 eV). Therefore, the DFT modelling suggests that the **N-DMBI** cation and radical anion species of the **NDI** derivatives form stable complexes due to their strong binding energies.[37] Importantly, the energy alignment between the complexes and their neural **NDI** derivatives enables an electron hopping process, and thus provides a route for effective n-type doping.

We next conducted a series of solid-state UV-vis absorption (Fig. 4) and conductivity (Fig. 5 and Tables S1, S2, ESI†) measurements of **NDI-G** and **NDI-EtHx** in terms of additive concentration and reaction time. The UV-vis absorption spectra in Fig. 4a and b illustrate the differing reaction times between the two **NDI** derivatives upon the addition of 50 mol% **N-DMBI**. Similar to the solution studies, new absorption peaks at 450 nm for **NDI-G**, and at 475 nm for **NDI-EtHx** are observed. **NDI-G** exhibited faster reaction kinetics than **NDI-EtHx**, with **NDI-G** displaying an absorption peak at 2 hours whereas it took approximately 24 hours **NDI-EtHx** to display a new absorption band. This slower doping process for **NDI-EtHx** is likely due to sluggish hydride transfer. In contrast, the glycol side-chain in **NDI-G** enhances its polarity and improves miscibility within the host/dopant blend.[16] This enhanced compatibility between **NDI-G** and **N-DMBI** molecules contributed to a more effective doping process compared to **NDI-EtHx**.[16,38–40] This observation aligns with previous reports, which have shown that an increase in reduction peak intensity in UV-vis absorption spectra correlates with the progression of the doping reaction time.[4,41]

However, the intensity of the UV-vis absorption spectrum of doped **NDI-G** declined after peaking at 2 hours, indicating a lack of stability of the resulting species. This decline is likely

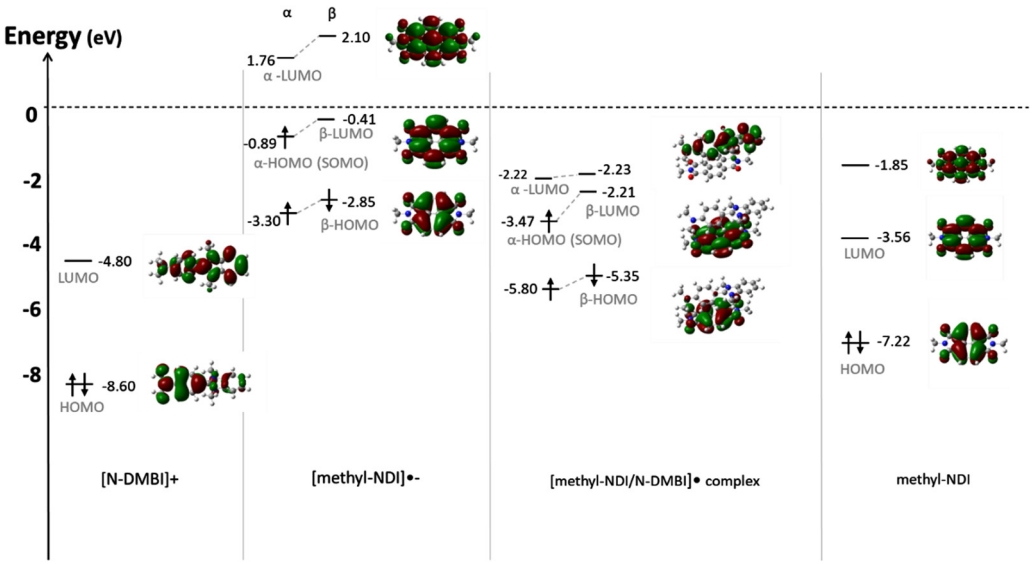


Fig. 3 DFT predicted HOMO/LUMO maps and energies of **[N-DMBI]**$^+$, **[methyl-NDI]**$^{\bullet-}$, **[methyl-NDI**$^-$**/N-DMBI**$^+$**]**$^\bullet$ complex and neutral **methyl-NDI**.

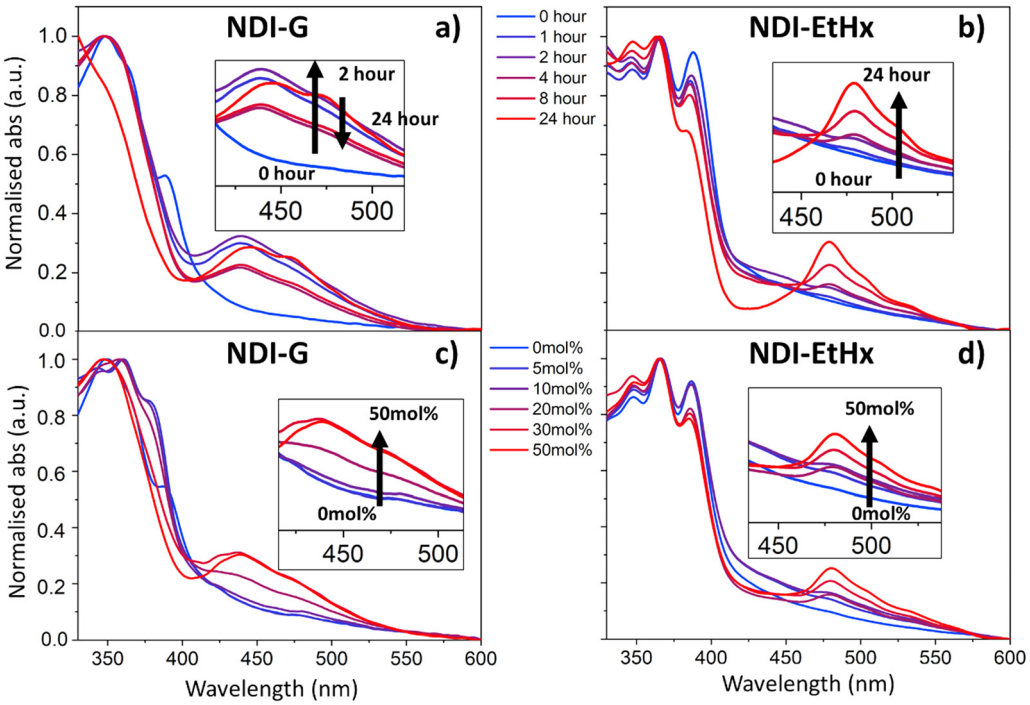


Fig. 4 UV-vis absorption spectra of (a) **NDI-G** and (b) **NDI-EtHx** in film on glass substrates with 50 mol% of **N-DMBI** in the presence of reaction times ranging from 0 to 24 hours; (c) **NDI-G** and (d) **NDI-EtHx** in film on glass substrates in the presence of 0 mol% to 50 mol%.

due to the highly reactive nature of organic radicals, which often leads to instability under ambient condition.[42] In contrast, **NDI-EtHx** exhibited a continuous increase in radical formation without a similar decline in intensity. Additional absorption measurements (Fig. S9, ESI†) confirm this radical instability, showing a reduction in the radical peak upon exposure to air.

The investigation was extended to demonstrate how increasing the mole percentages from 0 mol% to 50 mol% of **N-DMBI** influenced the doping process for **NDI-G** and **NDI-EtHx**. The new absorption peaks appeared from 20 mol% of **N-DMBI** doping for **NDI-G** and **NDI-EtHx**. As the concentration of **N-DMBI** was increased, the equilibrium position shifted towards the products, demonstrating a more pronounced doping reaction at higher dopant concentrations up to 50 mol%.

Conductivity measurements of **NDI** derivatives after the addition of 50 mol% **N-DMBI** added were performed to compare the doping efficiency with different side-chains, as shown in Fig. 5a. For **NDI-G**, the initial conductivity was low at $2.52 \times 10^{-7}$ S cm$^{-1}$ and significantly improved to $4.89 \times 10^{-4}$ S cm$^{-1}$ after 1 h. This enhancement reached its maximum value of $1.09 \times 10^{-3}$ S cm$^{-1}$ at the 2 h mark. After this point, the conductivity

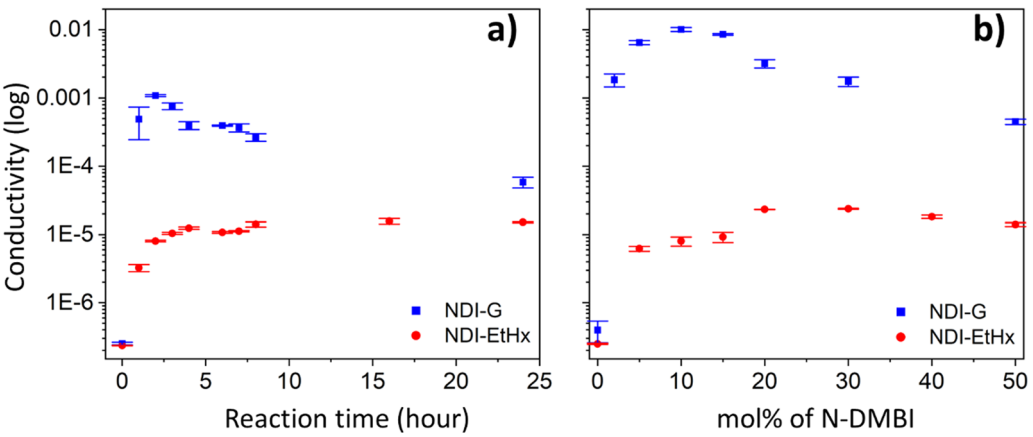


Fig. 5 Logarithmic plot of conductivity measurements for **N-DMBI** doped in **NDI-G** and **NDI-EtHx** at (a) reaction time ranging from 0 to 24 hours (50 mol% **N-DMBI** doping) and (b) ranging from 0 mol% to 50 mol% (reaction time: 2 hours for **NDI-G** and 16 hours for **NDI-EtHx**) (each data point represents the average of three samples with error bars).

 

declined to 5.8 × $10^{-5}$ S $cm^{-1}$ after 24 hours. In contrast, for **NDI-EtHx**, a 1 h reaction with **N-DMBI** led to an improvement in conductivity from an initial value of 2.35 × $10^{-7}$ S $cm^{-1}$ to 3.25 × $10^{-6}$ S $cm^{-1}$. The conductivity continued to increase to around $10^{-5}$ S $cm^{-1}$ and remained constant up to 24 hours. The results align with UV-vis absorption findings and suggest that the glycol side-chain provides a better environment for the n-type doping, allowing **NDI-G** to achieve maximum conductivity more quickly than **NDI-EtHx**. However, it is noteworthy that the conductivity in **NDI-G** dropped if the reaction was allowed to proceed for longer times.

Fig. 5b shows the conductivity for **NDI-G** and **NDI-EtHx** with varying mole percentages of **N-DMBI**, ranging from 0 mol% to 50 mol%, with reaction times determined from the maxima in Fig. 4a and b (**NDI-G** for 2 hours and **NDI-EtHx** for 16 hours). The initial conductivity of pristine **NDI-G** and **NDI-EtHx** ranged from 2 to 3 × $10^{-7}$ S $cm^{-1}$. In the case of **NDI-EtHx**, the conductivity increased to 6.21 × $10^{-6}$ S $cm^{-1}$ with 5 mol% **N-DMBI** and reached the maximum of 2.38 × $10^{-5}$ S $cm^{-1}$ at 30 mol%. However, the conductivity started to decline beyond this optimal additive concentration level, from 1.82 × $10^{-5}$ S $cm^{-1}$ at 40 mol% and further decreasing to 1.40 × $10^{-5}$ S $cm^{-1}$ at 50 mol%. In the case of **NDI-G**, the conductivity dramatically increased to 1.84 × $10^{-3}$ S $cm^{-1}$ with 2 mol% **N-DMBI** and peaked at 1.00 × $10^{-2}$ S $cm^{-1}$ with 10 mol% **N-DMBI** doping. However, a further increase in additive concentration led to a decline in conductivity, which dropped to 4.50 × $10^{-4}$ S $cm^{-1}$ at 50 mol%.

These results indicate that the successful doping of the **NDI** derivatives, with optimal conditions for **NDI-G** yielding conductivity values up to $10^{-2}$ S $cm^{-1}$. However, excessive additive concentration had a detrimental effect. High additive concentration levels likely introduce trap states within the material,[43,44] which can capture electrons and lead to a reduction in the electron conductivity[45,46] and mobility,[43,45] as well as increased recombination.[47] Consequently, this behaviour reduces the number of free charges within the material. Based on our results, the optimised doping conditions for these materials are: 10 mol% **N-DMBI** for a 2 h reaction for **NDI-G**, and 30 mol% **N-DMBI** for a 16 h reaction for **NDI-EtHx**. Notably, the doping kinetics of **NDI-G** are competitive with other materials, achieving peak conductivity within 3 hours.[41,48]

To evaluate the effectiveness of n-doping of **NDI** derivatives and their suitability in hybrid optoelectronic devices, we fabricated inverted PSCs with a configuration of glass/ITO/MeO-2PACz/$Al_2O_3$ NPs/perovskite/ETL/BCP/Ag. The performance of PSCs incorporating the pristine and doped **NDI** derivatives was compared to **PCBM**-based PSCs. Fig. 6 illustrates the *J*–*V* curves for these solar cells, while Table 1 provides a summary of their photovoltaic performance. Doping **NDI-G** with **N-DMBI** successfully enhances both conductivity and photovoltaic performance, with power conversion efficiency (PCE) increasing from 10.44% to 14.12%. After doping, the short circuit current density ($J_{sc}$) of **NDI-G** PSCs rises from 21.25 mA $cm^{-2}$ to 22.15 mA $cm^{-2}$, approaching the performance of **PCBM**-based PSCs. The improved conductivity in doped **NDI-G** facilitates better charge extraction towards the electrode, resulting in higher $J_{sc}$.

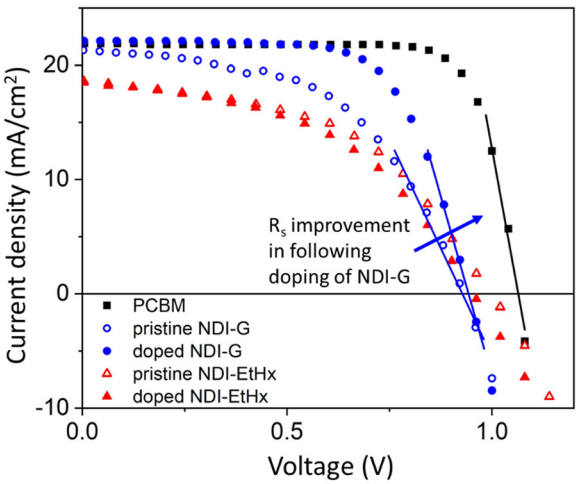


Fig. 6 *J*–*V* characteristics curves of **PCBM**, pristine and doped of **NDI-G** and **NDI-EtHx** based PSCs (lines represent to fitting curves of each *J*–*V* curves).

Table 1 Photovoltaic parameters of reference **PCBM**-based, pristine and doped **NDI-G**-based and **NDI-EtHx**-based PSCs

| ETL | N-DMBI (mol%) | $J_{sc}$ (mA $cm^{-2}$) | $V_{oc}$ (V) | FF | PCE (%) |
|---|---|---|---|---|---|
| **PCBM** | — | 21.86 ± 0.38 | 1.07 ± 0.01 | 0.78 ± 0.02 | 18.26 ± 0.69 |
| **NDI-G** | 0 | 21.25 ± 0.58 | 0.93 ± 0.06 | 0.53 ± 0.02 | 10.44 ± 0.80 |
| | 10 | 22.15 ± 1.14 | 0.94 ± 0.04 | 0.68 ± 0.07 | 14.12 ± 1.05 |
| **NDI-EtHx** | 0 | 18.56 ± 0.63 | 1.00 ± 0.07 | 0.50 ± 0.02 | 9.18 ± 0.83 |
| | 30 | 18.47 ± 1.43 | 0.95 ± 0.04 | 0.48 ± 0.02 | 8.45 ± 0.77 |

Additionally, the fill factor (FF) of doped **NDI-G** PSCs increased from 0.53 to 0.68 compared to undoped **NDI-G** PSCs. This enhancement is associated with a reduction of the series resistance, as evidenced by the slopes of the *J*–*V* curves, see Fig. 6. After doping, the values extracted for the series resistance are similar to **PCBM**-based PSCs, demonstrating the success of the approach. In contrast, doped **NDI-EtHx** does not exhibit any improvement in device performance. This lack of improvement is likely a result of the less effective doping process which does not yield a high enough conductivity value to overcome the detrimental effects of the addition of the dopant molecules.

However, despite the higher conductivity in doped **NDI-G** compared to **PBCM**, its overall performance is still lower than this reference system. Clearly, there are more elements at play at the interface than simple energy-level related arguments. In particular, there is a growing body of knowledge highlighting that fullerenes derivatives play additional roles to facilitate charge extraction, for instance in the form of surface passivation.[49] This effect is attributed to the interaction at the perovskite/**PCBM** interface, which reduces interfacial recombination and lowers the interfacial energy barrier.[50] Similar benefits have been observed in regular PSCs where $C_{60}$ self-assembled monolayers (SAMs) were used to passivate $SnO_2$, reducing interfacial defects.[51] This defect mitigation is further supported by minimized hysteresis in **PCBM**-based devices compared to **NDI**-based devices, as

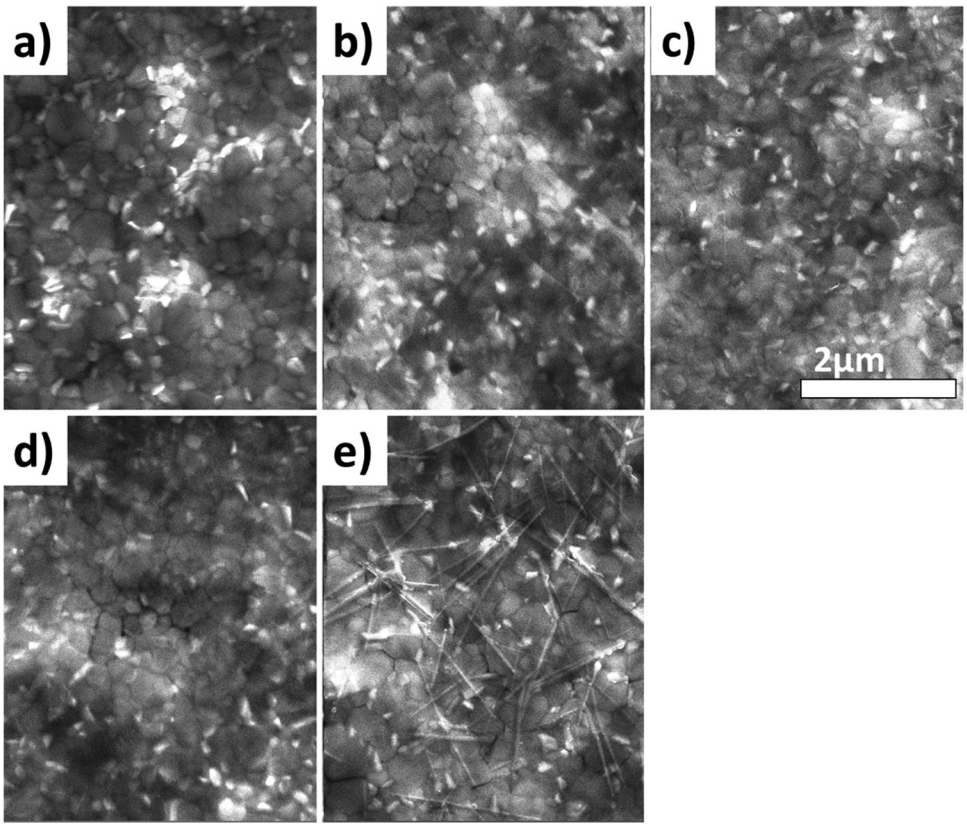


Fig. 7 SEM images of (a) **PCBM**; (b) pristine **NDI-G**; (c) pristine **NDI-EtHx**, (d) doped **NDI-G** and (e) doped **NDI-EtHx**.

shown in Fig. S10 (ESI†). Moreover, **PCBM** enhances performance by increasing $J_{sc}$, raising the shunt resistance ($R_{SH}$), and decreasing the series resistance ($R_s$), all of which contribute to an improved FF.

To further explore the reasons behind these performance differences, the film morphology was examined using scanning electron microscopy (SEM) (Fig. 7). No significant morphological changes were observed between **PCBM**, pristine **NDI-G**, and **NDI-EtHx**. After doping, the morphology of **NDI-G** remained unchanged, suggesting that the enhancement in solar cell performance can be attributed to increased charge transport as a result of the doping process. In contrast, doped **NDI-EtHx** exhibited the formation of needle-shaped features, suggesting that the dopant molecule may influence molecular packing or induce aggregation. The polarity difference between **NDI-EtHx** and **N-DMBI** likely leads to dopant residue aligning with the alkyl side-chain in crystalline regions. This disrupts the π–π stacking of **NDI** molecules or dopant self-aggregates, as observed in SEM images.[16] This behaviour is similar to that observed in reported **PCBM** systems,[52,53] where large aggregate formation negatively impacts solar cell performance. It is also possible that the steric hindrance of the alkyl side-chains in **NDI-EtHx** contributes to the aggregation. This explains why the open circuit voltage ($V_{oc}$) of doped **NDI-EtHx** decreased from 1.00 V to 0.95 V, likely due to surface recombination caused by the needle-shaped features, whereas **NDI-G** maintained a consistent $V_{oc}$ value.

## Conclusions

In this study, we have investigated two non-fullerene ETMs based on **NDI** analogues with solubility-enhancing side-chains: glycol (**NDI-G**) and alkyl (**NDI-EtHx**). The two **NDI** derivatives exhibit similar optical and electrochemical properties. Their initial pristine conductivities were low, and to address this, we employed n-type doping using **N-DMBI** as the dopant. However, the HOMO of **N-DMBI** is deeper than the LUMO of the **NDI** derivatives and thermal activation was required to generate the **NDI** radical anion species which was confirmed by EPR. DFT calculations suggest that complex formation occurs between the resulting **N-DMBI** cation and the **NDI** radical anion driven by strong binding energies. Importantly, energy alignment between the complex and neutral **NDI** molecules enables effective electron transfer to the latter, ultimately generating free charges. Through a series of UV-vis absorption and conductivity measurements, we observed that the polar glycol groups in **NDI-G** facilitate a faster doping reaction compared to the non-polar alkyl chains in **NDI-EtHx**. This difference is largely attributed to the polarity compatibility between the glycol side-chains and dopant within the film matrix, which promotes intermolecular interactions and enhances the doping reaction. Our optimised **NDI-G** doped material achieved a conductivity exceeding $10^{-2}$ S cm$^{-1}$. Integrating these derivatives in PSCs increased the PCE from 10.44% to 14.12% after **N-DMBI** doping, primarily by reducing the $R_s$. Although **NDI-G**

 

films outperform **PCBM** in terms of conductivity, the overall devices are less efficient than those with **PCBM** due to higher interfacial recombination which also leads to increased hysteresis. This indicates that interface passivation is more critical than reducing $R_s$ in the charge extraction layer. Overall, these findings further underscore the importance of side-chain engineering in the design of new dopant/semiconductor combinations.

## Author contributions

WKY and BV performed the analytical and device studies. LM, DW and MC synthesised and purified **NDI-G** and **NDI-EtHx**. LM and DW performed DFT calculations. MG performed SEM measurements. SS recorded the ESI spectra. GC and PD conceived and supervised the research project. All authors contributed to the writing and reviewing of this manuscript.

## Data availability

The data supporting this article have been included as part of the ESI.†

## Conflicts of interest

There are no conflicts of interests.

## Acknowledgements

WKY and MG thank the University of Glasgow for a College of Science and Engineering PhD scholarship. GC thanks Leverhulme Trust for a Research Fellowship and the EPSRC (EP/E036244/1). MC, DW and GC thank EPSRC (EP/V027425/1). PD acknowledges EP/T010568/1.

## References

1 T. H. Kim, J. H. Kim and K. Kang, *Jpn J. Appl. Phys.*, 2023, **62**, SE0803.
2 J. Liu, B. van der Zee, R. Alessandri, S. Sami, J. Dong, M. I. Nugraha, A. J. Barker, S. Rousseva, L. Qiu, X. Qiu, N. Klasen, R. C. Chiechi, D. Baran, M. Caironi, T. D. Anthopoulos, G. Portale, R. W. A. Havenith, S. J. Marrink, J. C. Hummelen and L. J. A. Koster, *Nat. Commun.*, 2020, **11**, 5694.
3 J. Song, F. J. Xu, X. D. Yan, F. Lin, C. C. Huang, L. P. You, T. J. Yu, X. Q. Wang, B. Shen, K. Wei and X. Y. Liu, *Appl. Phys. Lett.*, 2010, **97**, 232106.
4 L. Hu, T. Liu, J. Duan, X. Ma, C. Ge, Y. Jiang, F. Qin, S. Xiong, F. Jiang, B. Hu, X. Gao, Y. Yi, Y. Zhou, L. Hu, T. F. Liu, J. S. Duan, Y. Y. Jiang, F. Qin, S. X. Xiong, F. Y. Jiang, B. Hu, Y. H. Zhou, X. Y. Ma, Y. P. Yi, C. W. Ge and X. K. Gao, *Adv. Funct. Mater.*, 2017, **27**, 1703254.
5 Z. Wang, D. P. McMeekin, N. Sakai, S. van Reenen, K. Wojciechowski, J. B. Patel, M. B. Johnston, H. J. Snaith, Z. Wang, D. P. McMeekin, N. Sakai, S. van Reenen, K. Wojciechowski, J. B. Patel, M. B. Johnston and H. J. Snaith, *Adv. Mater.*, 2017, **29**, 1604186.
6 S. K. Jung, J. H. Heo, D. W. Lee, S. C. Lee, S. H. Lee, W. Yoon, H. Yun, S. H. Im, J. H. Kim and O. P. Kwon, *Adv. Funct. Mater.*, 2018, **28**, 1800346.
7 M. Korzec, S. Kotowicz, K. Łaba, M. Łapkowski, J. G. Małecki, K. Smolarek, S. Maćkowski and E. Schab-Balcerzak, *Eur. J. Org. Chem.*, 2018, 1756–1760.
8 D. Zhao, Q. Jiang, Y. Jia, J. Zhou, N. Zheng, D. Hu and Y. Ma, *Mater. Today Energy*, 2021, **21**, 100710.
9 D. Kiefer, A. Giovannitti, H. Sun, T. Biskup, A. Hofmann, M. Koopmans, C. Cendra, S. Weber, L. J. Anton Koster, E. Olsson, J. Rivnay, S. Fabiano, I. McCulloch and C. Müller, *ACS Energy Lett.*, 2018, **3**, 278–285.
10 D. Wang, T. Ye and Y. Zhang, *J. Mater. Chem. A*, 2020, **8**, 20819–20848.
11 S. K. Jung, J. H. Heo, D. W. Lee, S. H. Lee, S. C. Lee, W. Yoon, H. Yun, D. Kim, J. H. Kim, S. H. Im and O. P. Kwon, *ChemSusChem*, 2019, **12**, 224–230.
12 J. L. Wu, W. K. Huang, Y. C. Chang, B. C. Tsai, Y. C. Hsiao, C. Y. Chang, C. T. Chen and C. T. Chen, *J. Mater. Chem. A*, 2017, **5**, 12811–12821.
13 P. Karuppuswamy, C. Hanmandlu, K. M. Boopathi, P. Perumal, C. C. Liu, Y. F. Chen, Y. C. Chang, P. C. Wang, C. S. Lai and C. W. Chu, *Solar Energy Mater. Solar Cells*, 2017, **169**, 78–85.
14 J. Hyuck Heo, S.-C. Lee, S.-K. Jung, O.-P. Kwon and S. H. Im, *J. Mater. Chem. A*, 2017, **13**, 20615–20622.
15 L. M. Svirskaite, S. Mandati, N. Spalatu, V. Malinauskiene, S. Karazhanov, V. Getautis and T. Malinauskas, *Synth. Met.*, 2022, **291**, 117214.
16 J. Liu, L. Qiu, G. Portale, S. Torabi, M. C. A. Stuart, X. Qiu, M. Koopmans, R. C. Chiechi, J. C. Hummelen, L. Jan and A. Koster, *Nano Energy*, 2018, **52**, 183–191.
17 M. Comin, V. Lemaur, A. Giunchi, D. Beljonne, X. Blase and G. D'Avino, *J. Mater. Chem. C*, 2022, **10**, 13815–13825.
18 V. Vijayakumar, E. Zaborova, L. Biniek, H. Zeng, L. Herrmann, A. Carvalho, O. Boyron, N. Leclerc and M. Brinkmann, *ACS Appl. Mater. Interfaces*, 2019, **11**, 4942–4953.
19 M. Lenes, G.-J. A. H. Wetzelaer, F. B. Kooistra, S. C. Veenstra, J. C. Hummelen and P. W. M. Blom, *Adv. Mater.*, 2008, **20**, 2116–2119.
20 M. Khalid, M. Khan, K. Mahmood, M. Arshad, M. Imran, A. A. C. Braga and R. Hussain, *Sci. Rep.*, 2022, **12**, 20220.
21 P. Wei, J. H. Oh, G. Dong and Z. Bao, *J. Am. Chem. Soc.*, 2010, **132**, 8852–8853.
22 D. D. Tanner and J. J. Chen, *J. Org. Chem.*, 1989, **54**, 3842–3846.
23 D. D. Tanner, J. J. Chen, L. Chen and C. Luelo, *J. Am. Chem. Soc.*, 1991, **113**, 8074–8081.
24 O. Bardagot, C. Aumaître, A. Monmagnon, J. Pécaut, P.-A. Bayle and R. Demadrille, *Appl. Phys. Lett.*, 2021, **118**, 203904.
25 S. Riera-Galindo, A. Orbelli Biroli, A. Forni, Y. Puttisong, F. Tessore, M. Pizzotti, E. Pavlopoulou, E. Solano, S. Wang,

G. Wang, T. P. Ruoko, W. M. Chen, M. Kemerink, M. Berggren, G. Di Carlo and S. Fabiano, *ACS Appl. Mater. Interfaces*, 2019, **11**, 37981–37990.
26 Y. S. Shi, D. D. Yang, T. Xiao, Z. G. Xia, Y. H. Fang and X. J. Zheng, *Chem. Eng. J.*, 2023, **472**, 145152.
27 S. Caby, L. M. Bouchet, J. E. Argüello, R. A. Rossi and J. I. Bardagi, *ChemCatChem*, 2021, **13**, 3001–3009.
28 A. Mityashin, Y. Olivier, T. Van Regemorter, C. Rolin, S. Verlaak, N. G. Martinelli, D. Beljonne, J. Cornil, J. Genoe and P. Heremans, *Adv. Mater.*, 2012, **24**, 1535–1539.
29 A. D. Scaccabarozzi, A. Basu, F. Aniés, J. Liu, O. Zapata-Arteaga, R. Warren, Y. Firdaus, M. I. Nugraha, Y. Lin, M. Campoy-Quiles, N. Koch, C. Müller, L. Tsetseris, M. Heeney and T. D. Anthopoulos, *Chem. Rev.*, 2022, **122**, 4420–4492.
30 S. Jhulki, H. I. Un, Y. F. Ding, C. Risko, S. K. Mohapatra, J. Pei, S. Barlow and S. R. Marder, *Chemistry*, 2021, **7**, 1050–1065.
31 B. D. Naab, S. Guo, S. Olthof, E. G. B. Evans, P. Wei, G. L. Millhauser, A. Kahn, S. Barlow, S. R. Marder and Z. Bao, *J. Am. Chem. Soc.*, 2013, **135**, 15018–15025.
32 X. Q. Zhu, M. T. Zhang, A. Yu, C. H. Wang and J. P. Cheng, *J. Am. Chem. Soc.*, 2008, **130**, 2501–2516.
33 S. Yamamoto, T. Sakurai, L. Yingjin and Y. Sueishi, *Phys. Chem. Chem. Phys.*, 1999, **1**, 833–837.
34 B. D. Naab, S. Zhang, K. Vandewal, A. Salleo, S. Barlow, S. R. Marder, Z. Bao, B. D. Naab, Z. Bao, S. Zhang, S. Barlow, S. R. Marder, K. Vandewal and A. Salleo, *Adv. Mater.*, 2014, **26**, 4268–4272.
35 K. Al Kurdi, S. A. Gregory, S. Jhulki, M. Conte, S. Barlow, S. K. Yee and S. R. Marder, *Mater. Adv.*, 2020, **1**, 1829–1834.
36 M. L. Tietze, J. Benduhn, P. Pahner, B. Nell, M. Schwarze, H. Kleemann, M. Krammer, K. Zojer, K. Vandewal and K. Leo, *Nat. Commun.*, 2018, **9**, 1182.
37 F. Pallini, S. Mattiello, N. Manfredi, S. Mecca, A. Fedorov, M. Sassi, K. Al Kurdi, Y. F. Ding, C. K. Pan, J. Pei, S. Barlow, S. R. Marder, T. Q. Nguyen and L. Beverina, *J. Mater. Chem. A*, 2023, **11**, 8192–8201.
38 J. Liu, M. P. Garman, J. Dong, B. Van Der Zee, L. Qiu, G. Portale, J. C. Hummelen and L. J. A. Koster, *ACS Appl. Energy Mater.*, 2019, **2**, 6664–6671.
39 J. Liu, S. Maity, N. Roosloot, X. Qiu, L. Qiu, R. C. Chiechi, J. C. Hummelen, E. von Hauff and L. J. A. Koster, *Adv. Electron. Mater.*, 2019, **5**, 1800959.
40 J. Liu, L. Qiu, R. Alessandri, X. Qiu, G. Portale, J. Dong, W. Talsma, G. Ye, A. Akbar Sengrian, P. C. T. Souza, M. Antonietta Loi, R. C. Chiechi, S. J. Marrink, J. C. Hummelen, L. Jan Anton Koster, J. Liu, L. Qiu, R. Alessandri, X. Qiu, G. Portale, J. Dong, W. Talsma, G. Ye, A. A. Sengrian, M. A. Loi, R. C. Chiechi, S. J. Marrink, J. C. Hummelen, L. J. A. Koster and P. C. T. Souza, *Adv. Mater.*, 2018, **30**, 1704630.
41 S. Wang, H. Sun, U. Ail, M. Vagin, P. O. Å. Persson, J. W. Andreasen, W. Thiel, M. Berggren, X. Crispin, D. Fazzi and S. Fabiano, *Adv. Mater.*, 2016, **28** 10764–10771.
42 Q. Song, F. Li, Z. Wang and X. Zhang, *Chem. Sci.*, 2015, **6**, 3342–3346.
43 G. Zuo, Z. Li, O. Andersson, H. Abdalla, E. Wang and M. Kemerink, *J. Phys. Chem. C*, 2017, **121**, 7767–7775.
44 H. F. Haneef, A. M. Zeidell and O. D. Jurchescu, *J. Mater. Chem. C*, 2020, **8**, 759–787.
45 S. Olthof, S. Mehraeen, S. K. Mohapatra, S. Barlow, V. Coropceanu, J.-L. Brédas, S. R. Marder and A. Kahn, *Phys. Rev. Lett.*, 2012, **109**, 176601.
46 B. Lü, M. Riede and K. Leo, *Phys. Status Solidi A*, 2007, **210**, 9–43.
47 X. Ma, R. A. J. Janssen and G. H. Gelinck, *Adv. Mater. Technol.*, 2023, **8**, 2300234.
48 T. L. Dexter Tam, T. T. Lin, M. I. Omer, X. Wang and J. Xu, *J. Mater. Chem. A*, 2020, **8**, 18916–18924.
49 A. F. Akbulatov, O. A. Kraevaya, V. S. Bolshakova, L. A. Frolova and P. A. Troshin, *Synth. Met.*, 2023, **299**, 117468.
50 W. Zhang, Y.-C. Wang, X. Li, C. Song, L. Wan, K. Usman, J. Fang, W. Zhang, Y. Wang, X. Li, C. Song, L. Wan, K. Usman and J. Fang, *Adv. Sci.*, 2018, **5**, 1800159.
51 C. Wang, D. Zhao, C. R. Grice, W. Liao, Y. Yu, A. Cimaroli, N. Shrestha, P. J. Roland, J. Chen, Z. Yu, P. Liu, N. Cheng, R. J. Ellingson, X. Zhao and Y. Yan, *J. Mater. Chem. A*, 2016, **4**, 12080–12087.
52 S. Sung Kim, S. Bae and W. Ho Jo, *Chem. Commun.*, 2015, **51**, 17413.
53 J. H. Bae, Y. J. Noh, M. Kang, D. Y. Kim, H. Bin Kim, S. H. Oh, J. M. Yun and S. I. Na, *RSC Adv.*, 2016, **6**, 64962–64966.

 